Chinese Chemical Letters 35 (2024) 109330

Contents lists available at ScienceDirect

Chinese Chemical Letters

journal homepage: www.elsevier.com/locate/cclet

Double-layered skeleton of Li alloy anchored on 3D metal foam enabling ultralong lifespan of Li anode under high rate

Chaohui Wei[a], Zeyu Yao[a,b], Jin Ruan[a,b], Zhicui Song[a,b], Aijun Zhou[a,b], Yingze Song[c,*], Donghuang Wang[a], Jicheng Jiang[a], Xin Wang[a], Jingze Li[a,b,*]

[a] *Yangtze Delta Region Institute (Huzhou), University of Electronic Science and Technology of China, Huzhou 313000, China*
[b] *School of Materials and Energy, University of Electronic Science and Technology of China, Chengdu 611731, China*
[c] *State Key Laboratory of Environmental-Friendly Energy Materials, Tianfu Institute of Research and Innovation, School of Materials and Chemistry, Southwest University of Science and Technology, Mianyang 621010, China*

ARTICLE INFO

Article history:
Received 10 October 2023
Revised 12 November 2023
Accepted 21 November 2023
Available online 22 November 2023

Keywords:
Double-layered skeleton
Li alloy
3D Metal foam
Ultralong lifespan
Lithium metal batteries
High rate

ABSTRACT

The high specific capacity and low negative electrochemical potential of lithium metal anodes (LMAs), may allow the energy density threshold of Li metal batteries (LMBs) to be pushed higher. However, the existing detrimental issues, such as dendritic growth and volume expansion, have hindered the practical implementation of LMBs. Introducing three-dimensional frameworks (*e.g.,* copper and nickel foam), have been regarded as one of the fundamental strategies to reduce the local current density, aiming to extend the Sand' time. Nevertheless, the local environment far from the skeleton is almost the same as the typical plane Li, due to macroporous space of metal foam. Herein, we built a double-layered 3D current collector of Li alloy anchored on the metal foam, with micropores interconnected macropores, *via* a viable thermal infiltration and cooling strategy. Due to the excellent electronic and ionic conductivity coupled with favorable lithiophilicity, the Li alloy can effectively reduce the nucleation barrier and enhance the Li^+ transportation rate, while the metal foam can role as the primary promotor to enlarge the surface area and buffer the dimensional variation. Synergistically, the Li composite anode with hierarchical structure of primary and secondary scaffolds realized the even deposition behavior and minimum volume expansion, outputting preeminent prolonged cycling performances under high rate.

The emerging demands for the high-mileage electrical vehicles and large-scale renewables depository have driven the rapid development of advanced energy storage systems, with high energy densities, accompanied by a rigid requirement of safety and stability. However, the available lithium-ion batteries (LIBs) were restricted by the theoretical limit of state-of-the-art graphite/silicon based anodes (339 mAh/g, 747 mAh/cm^3) [1–3]. Consequently, the commercial batteries normally achieved the energy density of 256 Wh/kg and 697 Wh/L (2015: Panasonic NCR18650GA cell) [4,5]. Recently, replacing a graphite-based anode by lithium (Li) metal can dramatically increase the anode energy density, since Li metal has been considered as the "Holy Grail" of anodes, with a theoretic specific capacity of 3860 mAh/g and 2050 mAh/L, coupled with the most negative electrochemical potential (−3.04 V *vs.* the standard hydrogen electrode) [6,7]. Hence, the metallic Li has been widely applied as anode material for the devices beyond LIBs (all solid-state batteries, Li–S, and Li-air batteries), with three to six times energy density relative to the current LIBs. Nevertheless, several notorious problems have been standing in the commercialization way of Li metal batteries (LMBs). Specifically, the hostless nature of Li and rough surface of most current collector would induce the random nucleation of Li^+, resulting in the continuous growth of Li dendrite. The large-sized dendritic Li can cause the volume expansion, solid electrolyte interface (SEI) cracking, and dead Li formation [8,9]. Inherently, such process can over-consume the active material including Li and electrolyte, and damage the integrity of separator. Externally, these phenomena can trigger the large overpotential, capacity loss, low coulombic efficiency (CE) and potential thermal runway [10]. Therefore, restraining the growth of Li dendrite is essential to accomplish the next-generation LMBs with high energy density and safety threshold.

To date, various tactics have been proposed to address the above-mentioned issues, including electrolyte modification, solid state electrolyte, artificial protective layer, 3D current collector, and Li alloys. According to the Sand' time model, these strategies can be categorized as: the interlayer modification towards rapid Li^+

* Corresponding authors.
E-mail addresses: yzsong@swust.edu.cn (Y. Song), lijingze@uestc.edu.cn (J. Li).

https://doi.org/10.1016/j.cclet.2023.109330
1001-8417/

migration and rational stress-release; introducing functional additive in electrolyte or localized high-concentration electrolytes, to improve the quality of SEI film; anchoring lithiophilic sites to reduce the nucleation barrier for homogenous growth of Li; increasing the surface area to reduce the effective current density and retard the dendritic growth; regulating the Li^+ distribution to avoid the fast depletion of Li^+ on the anode surface [11–14]. Among them, the former two strategies focus on enhancing the robustness of SEI film and modifying the Li nucleation in the interface, without the whole matrix. The nucleation inside the electrode is normally uneven and SEI film would eventually crack as the accumulation of dead Li; hence, it can only restrict the Li dendrite to a limited extent. The latter ones can fundamentally solve the issues throughout the whole electrode structure, as verified by numerous reports [15–17]. For instance, Chi *et al.* utilized a nickel foam as the conductive 3D host to obtain a composite anode of Li@Ni foam *via* thermal infusion, presenting a smooth voltage pattern with considerable hysteresis over 100 cycles (200 mV, 5.0 mA/cm^2). The modulate mechanical strength of the composite anode enabled a minimum dimension change (merely $\approx$3.1%), and herein the effective inhibition of dendrite formation [18]. However, Li metal is essentially unaffiliated to Ni foam; therefore, the nucleation barrier is relatively high, resulting in large overpotential and low CE [19,20]. On top of such situation, the decorations of 3D host with Li wettable components have come into the stage. Specifically, Sun's group has *in-situ* chemically transformed the inert copper surface into 3D wettable $Cu(OH)_2$ nanowires, easily thriving a functional 3D Li@CuLi host, with the improved cyclic and rate performances [21]. Similarly, Jiang and his collaborators applied the immersing strategy to prepare interwoven nickel(II)-dimethylglyoxime (Ni-DMG) nanowires on nickel foam, as a robust host for Li metal anodes [22]. In line with this, some researchers incorporated metal–organic framework-derived Co_3O_4 into nickel foam to achieve stable Li^+ storage, and the corresponding Li||Li symmetric cells can operate over 1000 h at 1.0 mA/cm^2, 1 mAh/cm^2 [23]. Of note, the pore sizes of those conventional metal foam hosts are usually around 100 μm [19,24]. Therefore, despite those modification on the 3D framework can improve the lithiophilicity of metal foam to a certain extent, the broad inner voids of metal foam were filled with pure Li, whose deposition/dissolution behaviors follow the intrinsic trend, particularly for the local region far from the skeleton of metal foam. Consequently, the volume expansion and uneven nucleation would unavoidably occur, after limited cycles. Besides, the size of those *in-situ*/*ex-situ* decorations were relatively small ($<$1 μm), tending to crumble over repetitive cycling [25–29]. More importantly, the additional lithiophilic components were normally inferior electrotonic and ionic conductor, causing incremental internal cell resistance [27,30]. Hence, it is highly desirable to develop secondary network inside the macropores of metal foam, with primary requirement of considerable electronic and ionic conductivity, coupled with high lithiophilicity and relatively large size. Given this, Li-riched alloy can be a proper candidate to be a multifunctional subsidiary nest inside the metal foam, to obtain advanced composite anodes.

Recently, Li-riched alloys, including Li-Sn, Li-Al, Li-B and Li-Mg have attracted extensive attentions, as a proper replacement for traditional Li anode, owing to the superior Li lithiophilicity, Li^+ diffusion coefficient, electronic conductivity, and high theoretical capacity [14,31,32]. Li-riched alloy, typically are composed of Li intermetallic compound/solid-solution phase as inherent skeleton, and pure Li metal phase as a reversible Li reservoir. Furthermore, the unique 3D structure of Li alloys can buffer the dimensional fluctuation to realize the improved electrochemical performance [33,34]. Liu and her collaborators prepared $Li_{22}Sn_5$ lithiophilic skeleton with Li phase implanted inside, *via* a thermal melting method, where the rod like $Li_{22}Sn_5$ acted as an inert framework and free metal Li accounted for ultra-high specific capacity. Owing to the high electrical conductivity and redox potential, the Li-riched Li-Sn alloy anode achieved the conformal deposition of Li metal, more stable SEI and lowered charge transfer resistance [35]. However, the complete volume expansion of Li-Sn alloy is as high as 676%, comparable to silicon-based anode, disadvantageous for structural stability of LMA. Alternatively, other alloys like Li-Zn, Li-Al and Li-Mg presenting lower expansion rate were investigated [32–34,36]. Li *et al.* reported a new Li anode with Li_9Al_4 and Li-Mg to enable the boosted surface stability, minimum volume variation and excellent rate capability. The symmetric cell with Li_9Al_4/Li-Mg alloy anode delivered a low polarization voltage of 18 mV and prolonged cycling stability at 1 mA/cm^2 and 1 mAh/cm^2, over 1600 h [36]. Of note, the practical application normally bears high standard for the batteries at high rate, to realize considerable energy retention over ultrafast charge/discharging. Impressively, Li alloys can totally answer to such strict requirements. For example, Yao and co-workers applied Li-Zn dual-phase alloy to build advanced Li anode with rapid electron/ion channels to balance the gap in between ionic and electronic resistance, leading to the even inside-out deposition of Li^+ in Li10Zn matrix. The symmetric cell with thus-thrived electrode can smoothly operate for 500 h, under the harsh testing parameter of 10 mA/cm^2, 10 mAh/cm^2, and the corresponding full cell with $Li_4Ti_5O_{12}$ can maintain a stable cycling for 3800 cycles at 1.0 C (capacity retention: 80%) [33]. Therefore, the Li alloy, as a combination of fine electronic and ionic conductor, can readily realize the spatial distribution of Li^+ throughout the electrode framework. Although Li alloy can self-assembled as a 3D network for Li plating/stripping, the mechanical strength is insufficient to cope with ultralong cycling test. In the extreme condition of large Li stripping, the Li alloy can be decomposed to provide additional Li source [34,37]. This function can be a savior in certain cases; however, the disintegration of Li alloy skeleton can cause the structural collapse and cell failure. Thus, rigid 3D nest like metal foam can be incorporated to avoid such potential risk, as well as homogenously distribute the Li alloy species.

With those considerations bearing in mind, we developed an advanced composite anode with double-layered skeleton, where the metal foam played the part as fundamental network to accommodate substantial Li alloy anchoring and Li deposition, while Li alloy served as a secondary framework of the preeminent electronic and ionic conductor. Through a facial thermal infusion strategy, the lithiophilic Li alloy components were readily and evenly nested inside the macropores of metallic foam (Li10Zn@Ni and Li-Al@Cu). The phase segregation occurred upon the cooling process, the LiZn and LiAl solid solution were *in-situ* formed, functionalizing as a secondary scaffold to fill the macropores with smaller micropores, guaranteeing the homogenous deposition in the local environment inside the voids of metal foam to the fullest extent. Owing to the double-layered network of our composite anode, the reduced local current density, lowered nucleation barrier, and fast Li^+ conduction were realized, leading to the depressed dendritic formation and minimum volume variation. Accordingly, the cell with Li10Zn@Ni foam exhibit the improved electrochemical performance from all due aspects. Specifically, the symmetric cell with Li10Zn@Ni foam can continuously run for 2000 cycles under 5 mA/cm^2 and 5 mAh/cm^2, whist the counter cell with Li@Ni failed merely after 400 cycles. Impressively, the Li10Zn@Ni electrode can exert ultralong lifespan of 1000 cycles at a harsher testing of 10 mA/cm^2, 10 mAh/cm^2. Similar phenomena happen in the cell with Li-Al@Cu foam. When pairing with LTO cathode, the full battery can deliver over 2000 cycles in a high rate of 5.0 C with a high capacity retention of 78% in ester-based electrolyte.

Fig. 1a illustrates the synthetic procedure of the composite anode of Li alloy anchored on 3D current collector (Ni and Cu foam), and the subsequent assembly with cathode for full LMBs. Briefly, Li

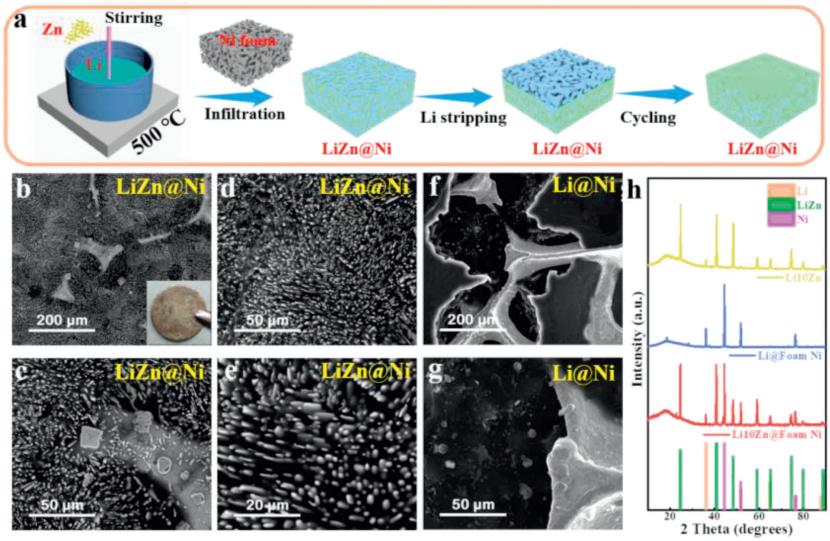

Fig. 1. (a) Schematic illustration of the preparation of Li10Zn@Ni composite and the corresponding cycling behavior. SEM images of (b-e) Li10Zn@Ni and (f, g) Li@Ni composite anode. (h) XRD profile of Li@Ni and Li10Zn@Ni foam. The insert in (b) is a digital photo of Li10Zn@Ni anode.

foil and metal particles were mixed in preset mass ratio, and then the clean metal foam was dipped into the molten metal slurry, for the rapid and complete impregnation of Li alloy. The composite electrode with double-layered framework was formed upon cooling down to room temperature. SEM measurement was performed to reveal the surface and inner morphology features of Li10Zn@Ni and Li-Al@Cu. Prior to the test, the three mass ratios, according to the phase diagram in Fig. S1 (Supporting information), were applied to obtain different LiZn alloys for optimization. SEM images of Li2Zn, Li10Zn and Li100Zn in Fig. S2 (Supporting information) revealed dense block morphology of surface of LiZn alloy began to occur, as the increase of Zn content. On the contrary, the LiZn strip started to appear while the mass proportion of Li rose. The number and size of block decreased while the density of needle increased, with free metal Li phase distributed inside. The massive and dispersive strip network tends to weaken the total structural integrity and strength. Hence, the dual-phase Li-riched Li10Zn alloy with the unique morphology of lump connecting massive branches was selected, owing to the accompanying fine mechanical robustness and large surface area, which can effectively resist the volumetric fluctuation and reduce the local current over cycling. Upon the incorporation the metal foam, the macropores of Ni framework were almost covered by dual phase of LiZn alloy and Li (Fig. S3 in Supporting information and Figs. 1b–e). Of note, the typical metal foam is barely affiliative to pristine Li metal, unless with additional treatment. Fortunately, the LiZn tends to grow tightly on skeleton of Ni foam, increasing the wettability of Ni towards Li [38,39]. As a result, the pore size of Ni foam markedly lowered, resulting in more uniform allocation of resting Li10Zn and Li metal phase. As exhibit in Figs. 1f and g, Ni foam can be distinctly observed with Li metal distributed inside.

The crystallinity and phase information on as-obtained electrode were probed by X-ray diffraction (XRD). The polymide (PI) protective type was utilized to cover the sample to prevent air oxidation; hence, the broad peak at around 10°−30° was attributed to PI film [35,40]. Upon the incorporation of Ni foam, there were still the pure combination of Li and Ni in Li@Ni foam from the characteristic XRD patterns, without new component appeared, indicating the sole role of Ni foam as an inert framework. The similar observation can be found in XRD curves of Li10Zn@Ni. Clearly, Li10Zn alloy merely consists of two phases: the cubic LiZn in-termetallic compound and Li metal, respectively with JCPDS No. 03-0954 and No. 15-0401 (Fig. 1h) [33,39,41]. These phenomena suggest the phase separation occurred upon the sudden drop of temperature, resulting in the formation of the dual-phase Li-riched LiZn alloy. Also, the absence of characteristic Zn peak indicates the complete reaction in between Li and Zn metal, additionally due to the excessive of Li.

Besides, the electrochemical stability of Ni foam was evaluated using cyclic voltammetry. A pair of redox peaks indexing to the deposition/dissolution of Li, were observed in the four cyclic voltammograms of tested anode, suggesting Ni foam solely acting as an inert supporting framework (Fig. S4 in Supporting information). In addition, the peak current (I_p) of four samples were compared and followed the trend bellows: I_p(Li10Zn)@Ni > I_p(Li10Zn) > I_p(Li)@Ni > I_p(Li). This clearly indicated 3D Li10Zn and Ni foam can significantly increase the active electro-active area and enhance the electron transmission, in-turn improving the cyclic performance especially under high rate [33,42]. After 1st cycle, I_p of Li10Zn anode gradually increased, as compared to Li electrode, due to more exposed active sites. The air stability of LiZn alloy electrode were also evaluated with electrochemical impedance spectroscopy (EIS) test. As shown in Fig. S5 and Table S1 (Supporting information), the impedance of cell with Li metal increased from initial value of 336–702 ohms in 10 days, as the continuous contact of Li with atmosphere and accompanying thickened SEI film. In stark contrast, the impedance of cell based on Li10Zn increased after 1 day, and gradually stabilized at around 400 ohms, with overall smaller resistance, as compared to pristine Li cell. This indicated the marked improvement of SEI film quality and charge transfer rate with LiZn alloy [43–46].

Similar operation was applied to investigate the Li-Al@Cu composite anode. The mass ratio for preparing LiAl alloy was optimized in our previous publication [34]. There were massive LiCu nanorods formed in Li@Cu, due to the alloy reaction over high-temperature heating and followingly immediate cooling down process (Fig. S6 in Supporting information). In contrast, Cu foam was inert and filled with dual phase of Li_9Al_4 and Li, during the fabrication of Li-Al@Cu composite anode (Fig. S7 in Supporting information). From XRD patterns in Fig. S8 (Supporting information), a slight Cu peak shift was observed in Li@Cu electrode, due to solid solution reaction in between Cu and Li [27,47]. As for Li-Al@Cu, the typical diffraction peaks of Li and Li_9Al_4 appeared without peak shift of Cu, demonstrating the Cu foam was an inert and stable

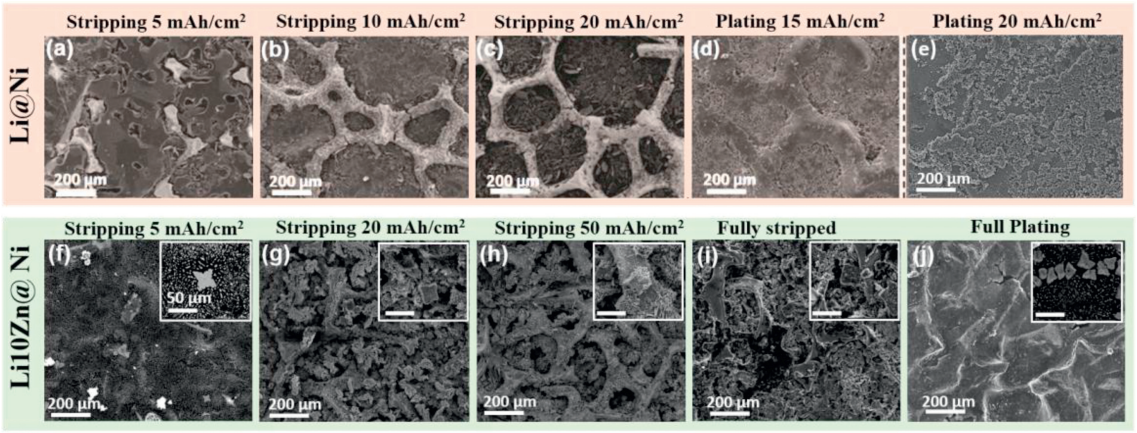

Fig. 2. SEM images of (a-e) Li@Ni and (f-j) Li10Zn@Ni composite anodes under different stripping and plating capacities. The insets are the enlarged SEM images of Li10Zn@Ni electrodes.

framework in the composite anode. Attributed to exceptional affinity in between LiAl alloy and Cu foam, Li_9Al_4 prioritized to be absorbed on the skeleton of Cu foam, other than molten Li metal, further transferring Cu foam from lithiophobicity into lithiophilicity [48]. Similar to the preparation of Li10Zn@Ni composite anode, phase separation occurred over sudden transfer of sample to room-temperature environment. Also, Al peak can be barely detected, indicative of complete dissolution of Al particles.

Furthermore, the morphologies and electrochemical performances of Li-Al@Cu and Li@Cu after chemical delithiation with deionized water were evaluated. Obviously, the surface of Cu skeleton was covered with residual LiCu nanowires, whilst Li_9Al_4 nanoclusters were observed in Li-Al@Cu, which could modify the surface affinity of Cu foam and regulate the deposition behavior of Li (Fig. S9 in Supporting information). Along with this, the half-cells with two types of washed framework were assembled to conduct CE test, under 1 mA/cm^2 and 1 mAh/cm^2. The overpotential of Li-Al@Cu (delithiated) and Li@Cu (delithiated) respectively were 23 and 68 mV, demonstrative of the reduced nucleation barrier, induced by more affiliative Li_9Al_4 nanoflower, as compared to LiCu nanowires (Fig. S10 in Supporting information) [20,49]. Accordingly, CE of Li-Al@Cu (delithiated) half-cell output a long lifespan of 140 cycles with an ultimate CE of 90% (Li@Cu: 80 cycles, 88%), indicative of enhanced Li utilization and optimized Li growth behavior induced from inert Cu structure and affinitive Li_9Al_4 alloy.

The morphology evolutions of the two composite anodes were estimated with SEM characterization, under an applied current density of 5 mA/cm^2. With the ongoing of delithiation process, the skeleton of Ni foam was gradually exposed from plane and sectional views (Figs. 2a–c and Figs. S11a–c, f-h in Supporting information). However, the surface of re-plated electrode was relatively rough, with slight dendrite formed after complete plating, due to hostless nature of Li metal, especially under high deposition capacity (Figs. 2d, e and i, j). Of note, the thickness of Li@Ni composite anode almost returned to the original state (Fig. S11a and e in Supporting information), fully verifying the effectiveness of primary Ni foam in reducing the local current density and buffering volume change, during the early cycling process. Regarding to the Li10Zn@Ni cell, the bare Ni foam framework with uniformly distributed LiZn alloy components were exposed after further gradual exfoliation of 20 and 50 mAh/cm^2 Li (Figs. 2f–h). The free Li in the voids of Li10Zn@Ni structure, including trenches and block edges of LiZn alloy, was successively dissolved. Upon the entire stripping, the Li10Zn components were disintegrated in to Zn particles (Fig. 2i), as confirmed by the XRD profiles in Fig. S12 (Supporting information), where only pure Zn and Ni signals were detected after full electrochemical delithiation. Accordingly, the specific capacity of Li10Zn@Ni electrode was calculated to be 1274.5 mAh/g, based on the whole electrode mass (Fig. S13 in Supporting information). Under a full-replating, the surface of Li10Zn@Ni showed relatively flat texture, suggestive of homogeneous and dense deposition (Fig. 2j). The probable reason is more active sites from LiZn alloy, as well as the reduced local current density from the enlarged surface area, owing to the double-layered skeleton of our composite anode. The alike observation can be obtained from the sectional views of Li@Cu and Li-Al@Cu composite anode in Fig. S14 (Supporting information). The LiCu nanowires and Li_9Al_4 clusters anchored on Cu foam framework were respectively disclosed in Li@Cu and Li-Al@Cu, along with the dissolution process (Figs. S14a–d). When the plating was applied, the Li@Cu anode displayed coarse texture, whilst the surface of Li-Al@Cu remained relatively smooth (Figs. S14e and f). Although certain amount of LiCu nanowires were formed during the thermal melting process, the lower nucleation barrier of LiAl, compared to LiCu alloy (also manifested in Fig. S10), can enable more effective and compact deposition [27,34,47].

As-prepared composite Li anodes were then tested using the Li||Li symmetric configuration, under the galvanostatic conditions. Under the current density of 1 mA/cm^2 and applied capacity of 1 mAh/cm^2 in ether-based electrolyte, the cell of Li10Zn@Ni composite electrode can stably operate for 2000 cycles (4000 h) with an ultralow voltage hysteresis of 10 mV (Fig. 3a). From the zoom-in view in Fig. 3b, the corresponding the curve can nearly sustain the typical crescent-shape without short-circuit. In stark contrast, the polarization voltage of Li@Ni anode increased with the cycling depth, attributed the increased migration resistance of Li^+. The cell failure occurred only after 800 cycles, due to Li dendrite piercing though the separator. With the rise of both applied current and areal capacity to 5 mA/cm^2 and 5 mAh/cm^2, the cell of Li10Zn@Ni can still smoothly run for 2000 cycles (4000 h), with the stabilized over-potential of 60 mV (Fig. 3c). The enlarged voltage profile displayed the arc shape, due to the accumulation of unavoidable powdery and “dead” Li (Fig. 3d) [50,51]. The counter cell only sustained for 400 cycles with the sharply increased voltage. In a harsher testing condition of 10 mA/cm^2 and 10 mAh/cm^2, the lifespan of symmetric cell of Li10Zn@Ni can again run for a long period of 1000 cycles (Figs. 3e and f). The cyclic life of Li10Zn@Ni composite anode was approximately doubled as compared to LiZn electrode in our previous report [30]. The cyclic behaviors of Li@Ni and Li10Zn@Ni were also measured in ester-based electrolyte (Fig. S15 in Supporting information), where the Li10Zn@Ni cell exceeded the Li@Ni cell in all tested conditions. The symmetric cell of Li@Cu and Li-Al@Cu were also followingly assembled. As shown in Figs. S16 and S17

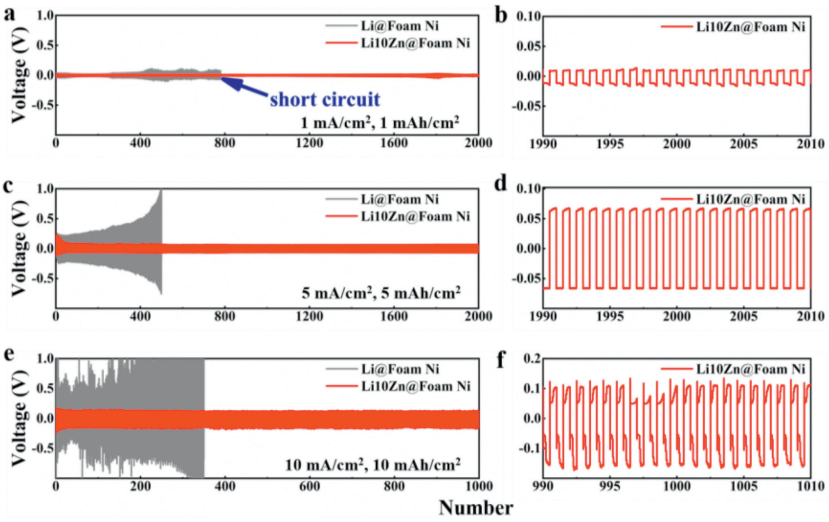

Fig. 3. Symmetric cells of Li@Ni and Li10Zn@Ni under (a, b) 1 mA/cm^2, 1 mAh/cm^2; (c, d) 5 mA/cm^2, 5 mAh/cm^2; (e, f) 10 mA/cm^2, 10 mAh/cm^2 in ether-based electrolyte.

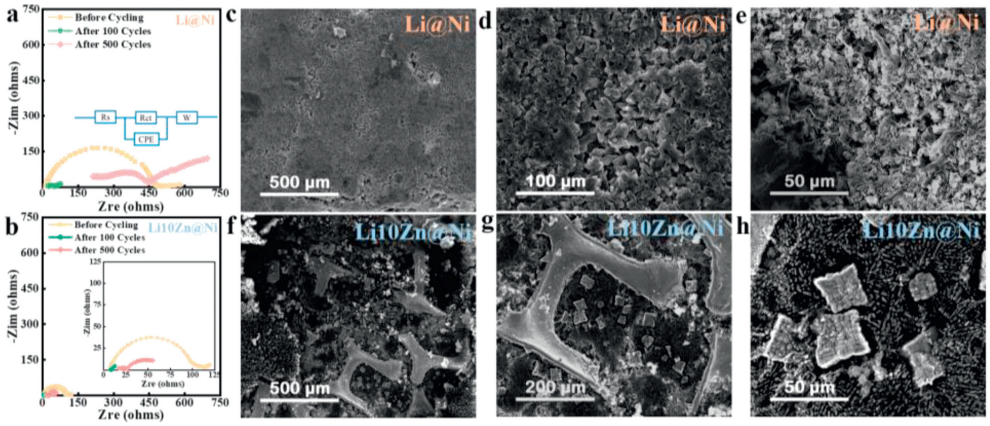

Fig. 4. EIS tests of symmetric cells of (a) Li@Ni and (b) Li10Zn@Ni. Post-Morten SEM images of (c-e) Li@Ni and (f-h) Li10Zn@Ni after 500 cycles.

(Supporting information), the cell with Li-Al@Cu electrode can run for 750 cycles, whilst the counter cell failed after 200 cycles with the fluctuated voltage, at 1 mA/cm^2 and 1 mAh/cm^2 in ester-based electrolyte. The cyclic performances of Li-Al@Cu cell also outperformed the Li cell, in harsher testing conditions. The post-morten EIS tests prior and after cycling were conducted to evaluate the evolution of internal resistance (Fig. S18 in Supporting information), where the R_{cell} of two cells became smaller along with cycling. Specifically, R_{cell} of Li-Al@Cu and Li@Cu cell markedly decreased to 23 and 42 ohms, separately, upon 20 cycles of activation process. With the cycling ongoing, R_{cell} of Li-Al@Cu remained almost constant, whilst the Li@Cu cell revealed an obvious increase in the value of R_{cell}. This indicates the dense and homogeneous deposition of Li^+, less side reactions, and robust SEI film, enabled the improved Li^+ transport and charge transfer in the composite anode with double-layered skeleton.

With regarding to Li10Zn@Ni and Li@Ni cells, the electrochemical impedance spectra after 100 and 500 cycles at 5 mA/cm^2 and 5 mAh/cm^2 were carried out (Figs. 4a and b). The initial resistances of two cells (R_{cell}) were 489 and 113 ohms, respectively for Li@Ni and Li10Zn@Ni electrodes. The lower value of Li10Zn@Ni composite can be ascribed to the superior electrical conductivity of LiZn alloy. After 100 cycles, Li@Ni and Li10Zn@Ni symmetric cells exhibit R_{cell} of 48 and 9 ohms, separately. The sharp decrease was due to the roughened surface along with cycling, and more exposed reaction sites in 3D Ni foam enabled the readier deposition of Li. Upon a long period of 500 cycles, the R_{cell} of Li@Ni sharply increased to 450 ohms, as the porous Li dendrite and cracked SEI film prolonged the transportation path of Li^+. Instead, Li10Zn@Ni cell exhibit a slightly increased R_{cell} of 26 ohms, ascribed to the firmly anchored Li10Zn block rationally regulating Li deposition. Acquired from the overall enhanced electrochemical performance, the probable reasons could be explained as follows: (1) The large surface area of *in-situ* formed Li alloy components could depress the local current density to avoid Li^+ agglomeration; (2) The lithiophilic nature of Li alloy transformed the inert surface of metal foam into wettable surface, reducing the nucleation barrier; (3) The high electric and ionic conductivity of Li alloy can enable the rapid Li transmission and reaction kinetics; (4) The dual-layered skeleton of metal foam and Li alloy synergistically realized a robust framework to buffer the volume expansion over cycling.

The postmortem SEM measurements were then conducted to characterize the surface state of composite Li electrode, upon disassembling the symmetric cells after cycling. Obviously, the surface of Li@Ni was completely covered by porous dead Li, indicative of the uneven Li^+ nucleation in Ni foam, particularly under crude testing condition (Fig. 4c). The moss and filamentous structure, displayed in magnified SEM images (Figs. 4d and e), can accelerate the cumulation of dead Li and constant loss of active Li, aggravating cell polarization. Surprisingly, the surface texture and morphology of Li10Zn@Ni was almost similar to the original state, due to uniform Li deposition and fast Li transportation (Figs. 4f–h). Simi-

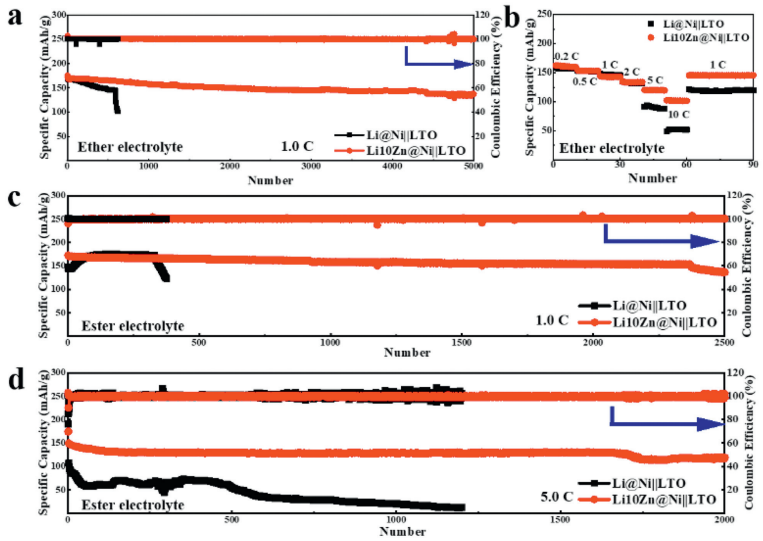

Fig. 5. (a) Cycling at 1.0 C and (b) rate performances of Li@Ni||LTO and Li10Zn@Ni||LTO in ether-based electrolyte. Long cyclic performances of Li@Ni||LTO and Li10Zn@Ni||LTO at (c) 1.0 and (d) 5.0 C in ester-based electrolyte.

lar observation can be found in postmortem SEM images of Li@Cu and Li-Al@Cu (Fig. S19 in Supporting information).

The commercial cathodes were paired with our composite anodes with double-layered skeleton to assemble the full cells, validating their practical feasibility. Fig. 5a displays the cycling performances of Li@Ni||($Li_4Ti_5O_{12}$) LTO and Li10Zn@Ni||LTO full cells at 1.0 C (1.0 C = 170 mA/g) in ether and ester electrolytes. The initial capacities of the two full cells were similar (170 mAh/g for Li@Ni||LTO; 173 mAh/g for Li10Zn@Ni||LTO). The Li10Zn@Ni||LTO cell can continuously run for 5000 cycles with a high capacity retention of 82.5%, whilst the capacity decay occurred merely after 550 cycles in the counter cell. This suggests the double-layered skeleton of Li10Zn@Ni can rationally regulate the Li deposition, as compared to single-layered framework of Li@Ni anode, therefore avoiding the formation of Li dendrite. From the rate performances in Fig. 5b, the output capacities of Li10Zn@Ni||LTO cell were higher, as compared to Li@Ni||LTO in the whole range of current densities. The capacity difference was even magnified in high rate, due to the fast ion transmission and lowered nucleation barrier in the double-layered skeleton of Li10Zn@Ni anode. The cyclic performance of full cells in ester-electrolyte was inferior, in contrast to ether electrolyte, under the same condition, due to more parasitic reactions (Fig. 5c). When the applied current increasing to 5.0 C in ester electrolyte, the full cell of Li10Zn@Ni||LTO can maintain a stabilized cycling performance for 1700 cycles at a capacity around 135 mAh/g (Fig. 5d). In stark contrast, a sudden drop happened after 150 cycles in Li@Ni||LTO battery. The double-layered skeleton structure of the composite anode cannot only reduce the local current density, but also accelerate the transportation rate of Li^+, due to the incorporation of LiZn alloy, thereby leading to homogenous deposition of Li and minimum volumetric fluctuation.

Analogously, Li-Al@Cu anode was assembled with the commercia cathode of $LiFePO_4$ (LFP), undergoing a cyclic test at 1.0 C in ester electrolyte (Fig. S20 in Supporting information). The Li-Al@Cu||LFP full battery achieved a relatively long lifespan of 400 cycles with the capacity retention of 85.2% (1^{st}: 142 mAh/g; 400^{th}: 121 mAh/g), distinctively longer as compared to Li@Cu ||LFP (1^{st}: 137 mAh/g; 240^{th}: 75 mAh/g, retention rate: 54.7%). Although the small amount of LiCu was formed during the preparation of Li@Cu, the lithiophilicity of LiCu was inferior to LiAl alloy; hence, dead Li generated after certain cycles, hindering the Li^+ transmission and increasing the cell resistance. Table S2 and Fig. S21 (Supporting information) collected the overall electrochemical performances of Li10Zn@Ni and Li-Al@Cu composite anodes with other state-of-the-art 3D Li anodes, displaying a distinct advance of our double-layered skeleton in enabling excellent anode with ultralong lifespan.

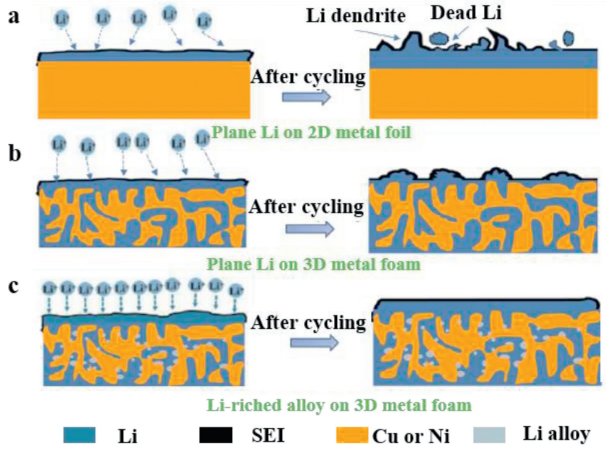

Fig. 6. Scheme of stripping and plating mechanism of Li, Li@metal foam and Li-riched alloy@metal foam (a–c).

According to the experimental analysis, the lithiation mechanism of the composite anode was schematically exhibit in Fig. 6. At the beginning of Li plating, Li^+ starts to migrate towards the anode surface under the dual effect of the electric field and concentration gradient. Owing to hostless nature of Li metal and rough surface of current collector, the heterogenic growth would normally occur, leading to the local accumulation of Li^+ and following dendrite formation. The dendritic Li would crack the SEI film and further aggravate the uneven deposition of Li, leading to the structural collapses of anode (Fig. 6a). When incorporating metal foam, the volumetric fluctuation is firstly buffered, due to the increased surface area and beneficial mechanical strength. The high electrical conductivity can enhance the electron transfer, and according Li redox kinetics. However, the lithiophobic nature of Cu/Ni foam would lead to the high nucleation barrier and large overpotential, as well as uncompact nucleation in the voids of metal foam. There-

fore, SEI fracture and dendritic growth would ultimately happen, resulting in large polarization of the battery (Fig. 6b). Along with this line, the surface of metal foam needs to be modified to resolve the plight. Followingly, the double-layered skeleton of the composite anode with tough structure of metal foam and affinitive Li alloy, can synergistically realize the increased reactive area and homogeneous deposition, leading to dense surface and minimum dimensional change after ultralong cycling (Fig. 6c).

In this work, the Li alloy skeletons were rationally nested in metal foam to build a multi-scale meshwork for the Li anode, upon the thermal molten and cooling treatment. We demonstrated two examples of such design in this work (Li10Zn@Ni and Li-Al@Cu foam), with the satisfied electrochemical performances. The local environment far from the skeleton of Ni foam was similar to plain Li metal, in the 3D composite anode with metal foam. In stark contrast, the Li10Zn with tree like morphology can role as secondary structure to split macropores of Ni foam, guaranteeing the local environment unit of Li nucleation was homogeneous, throughout the whole electrode matrix. The composite Li anode with double-layered skeleton with hierarchical pores can effectively depress the nucleation barrier, reduce the local current density, and improve the Li^+ diffusion rate, thereby realizing the even deposition behaviors and Li dendrite restraint. Accordingly, as-prepared Li10Zn@Ni composite anode can smoothly operate for 1000 cycles under the current density of 10 mA/cm^2 and areal capacity of 10 mAh/cm^2 in ether electrolyte. Accordingly, the full cell with LTO cathode outputs an excellent long-term cycling performance for 2000 cycles at 5.0 C in ester electrolyte. This work sheds light on the rational design of feasible and robust LMAs based on 3D framework for next-generation battery with ultralong lifespan.

Declaration of competing interest

The authors declare that they have no known competing financial interests or personal relationships that could have appeared to influence the work reported in this paper.

Acknowledgments

This work was supported by Huzhou Natural Science Foundation Project (Nos. 2022YZ04 and 2022YZ21), S&T Special Program of Huzhou (No. 2023GZ03) and National Natural Science Foundation of China (No. 52172184).

Supplementary materials

Supplementary material associated with this article can be found, in the online version, at doi:10.1016/j.cclet.2023.109330.

References

[1] A. Yang, C. Yang, K. Xie, et al., ACS Energy Lett. 8 (2023) 836–843.
[2] M. Zhu, X. Zhao, R. Yan, et al., Curr. Opin. Solid State Mater. 27 (2023) 101079.
[3] S. Kim, G. Park, S.J. Lee, et al., Adv. Mater. 35 (2023) 2206625.
[4] R. Schmuch, R. Wagner, G. Hörpel, et al., Nat. Energy 3 (2018) 267–278.
[5] T. Placke, R. Kloepsch, S. Dühnen, et al., J. Solid State Electrochem. 21 (2017) 1939–1964.
[6] C.Y. Wang, T. Liu, X.G. Yang, et al., Nature 611 (2022) 485.
[7] R. Zhang, X. Chen, X. Shen, et al., Joule 2 (2018) 764–777.
[8] Z. Zhu, T. Jiang, M. Ali, et al., Chem. Rev. 122 (2022) 16610–16751.
[9] S. Weng, X. Zhang, G. Yang, et al., Nat. Commun. 14 (2023) 4474.
[10] Z. Piao, R. Gao, Y. Liu, et al., Adv. Mater. 35 (2023) 2206009.
[11] J.X. Liu, N.B. Pei, X.Y. Yang, et al., Energy Mater. 3 (2023) 300024.
[12] C.Y. Lu, M. Tian, X.J. Zheng, et al., Chem. Eng. J. 430 (2022) 132722.
[13] J. Li, Z. Kong, X. Liu, et al., InfoMat 3 (2021) 1333–1363.
[14] X. Gu, J. Dong, C. Lai, Eng. Rep. 3 (2021) e12339.
[15] Q. Wang, B. Liu, Y. Shen, et al., Adv. Sci. 8 (2021) 2101111.
[16] X.B. Cheng, R. Zhang, C.Z. Zhao, et al., Chem. Rev. 117 (2017) 10403–10473.
[17] A. Hu, F. Li, W. Chen, et al., Adv. Energy Mater. 12 (2022) 2202432.
[18] S.S. Chi, Y. Liu, W.L. Song, et al., Adv. Funct. Mater. 27 (2017) 1700348.
[19] J. Cao, L. Deng, X. Wang, et al., Energy Fuels 34 (2020) 7684–7691.
[20] J. Qian, S. Wang, Y. Li, et al., Adv. Funct. Mater. 31 (2021) 2006950.
[21] K.R. Adair, M. Iqbal, C. Wang, et al., Nano Energy 54 (2018) 375–382.
[22] T. Zhou, Y. Mu, J. Wu, et al., Chin. Chem. Lett. 33 (2022) 2165–2170.
[23] T. Wei, J. Lu, P. Zhang, et al., Chin. Chem. Lett. 34 (2023) 107947.
[24] X.Y. Yue, W.W. Wang, Q.C. Wang, et al., Energy Storage Mater. 21 (2019) 180–189.
[25] B.C. Ding, X.F. An, J. Yu, et al., Energy Mater 2 (2022) 200039.
[26] J.B. Hou, K. Zhang, J.H. Xiao, et al., Tungsten 4 (2022) 356–369.
[27] Z.H. Wang, J. Xue, Y.C. Liu, et al., Sci. China Mater. 65 (2022) 69–77.
[28] Y.F. Ding, Y.J. Sun, Z.X. Shi, et al., Small Struct. 4 (2023) 2200313.
[29] Z.X. Shi, Z.T. Sun, X.Z. Yang, et al., Small Sci. 2 (2022) 2100110.
[30] Y. Fan, H. Li, X. He, et al., ACS Appl. Energy Mater. 5 (2022) 10034–10044.
[31] B. Sun, Y. Xu, S. Yang, et al., Mater. Chem. Front. 7 (2023) 2554–2569.
[32] M. Peng, K. Shin, L. Jiang, et al., Angew. Chem. Int. Ed. 61 (2022) e202206770.
[33] Z.Y. Yao, W.S. Jia, Z.H. Wang, et al., J. Energy Chem. 51 (2020) 285–292.
[34] C.H. Wei, J. Ruan, Z.C. Song, et al., J. Alloy. Compd. 960 (2023) 170643.
[35] Y.C. Liu, T. Chen, J. Xue, et al., Electrochim. Acta 405 (2022) 139787.
[36] Y. Li, J. Li, H. Xiao, et al., Adv. Funct. Mater. 33 (2023) 2213905.
[37] Z.H. Wang, Y.C. Liu, J.X. Xing, et al., Research 2022 (2022) 9843093.
[38] L. Qin, H. Xu, D. Wang, et al., ACS Appl. Mater. Interfaces 10 (2018) 27764–27770.
[39] J. Bao, H.J. Pei, X.Y. Yue, et al., Nano Res. 16 (2023) 8345–8353.
[40] Y. Zhang, H. Wang, Y. Yang, et al., Chem. Eng. J. 461 (2023) 141993.
[41] Y. Ouyang, C. Cui, Y. Guo, et al., ACS Appl. Mater. Interfaces 12 (2020) 25818–25825.
[42] C.H. Wei, M. Tian, Z.D. Fan, et al., Energy Storage Mater. 41 (2021) 141–151.
[43] S. Zhang, Q. Sun, G. Hou, et al., Nano Res. 16 (2022) 6825–6832.
[44] P. Qing, Z.B. Wu, A.B. Wang, et al., Adv. Mater. 35 (2023) 2211203.
[45] K.Q. Geng, M.Q. Yang, J.X. Meng, et al., Tungsten 4 (2022) 323–335.
[46] S.Y. Liu, Y.H. Zhou, Y.B. Zhang, et al., Tungsten 4 (2022) 336–345.
[47] W.S. Jia, Y.C. Liu, Z.H. Wang, et al., Sci. Bull. 65 (2020) 1907–1915.
[48] T. Chen, J.J. S, J.X. Xing, et al., ACS Appl. Energy Mater. 4 (2021) 4879–4886.
[49] S.J. Yang, N. Yao, F.N. Jiang, et al., Angew. Chem. Int. Ed. 61 (2022) e202214545.
[50] K.H. Chen, K.N. Wood, E. Kazyak, et al., J. Mater. Chem. A 5 (2017) 11671–11681.
[51] C. Jin, T. Liu, O. Sheng, et al., Nat. Energy 6 (2021) 378–387.